Nuclear Engineering and Technology 51 (2019) 238–248

Contents lists available at ScienceDirect

Nuclear Engineering and Technology

journal homepage: www.elsevier.com/locate/net

Original Article

# Three-dimensional numerical simulation of hydrogen-induced multi-field coupling behavior in cracked zircaloy cladding tubes

Zhongjia Xia [a], Bingzhong Wang [a], Jingyu Zhang [a], Shurong Ding [a, *], Liang Chen [b], Hua Pang [b], Xiaoming Song [b]

[a] Institute of Mechanics and Computational Engineering, Department of Aeronautics and Astronautics, Fudan University, Shanghai 200433, China
[b] Science and Technology on Reactor System Design Technology Laboratory, Nuclear Power Institution of China, Chengdu 610041, Sichuan, China

ARTICLE INFO

*Article history:*
Received 15 July 2018
Received in revised form
31 August 2018
Accepted 25 September 2018
Available online 27 September 2018

*Keywords:*
Numerical simulation
Multi-field coupling
DHC
Irradiation effects
Hydride-precipitation-induced effects

ABSTRACT

In the high-temperature and high-pressure irradiation environments, the multi-field coupling processes of hydrogen diffusion, hydride precipitation and mechanical deformation in Zircaloy cladding tubes occur. To simulate this hydrogen-induced complex behavior, a multi-field coupling method is developed, with the irradiation hardening effects and hydride-precipitation-induced expansion and hardening effects involved in the mechanical constitutive relation. The out-pile tests for a cracked cladding tube after irradiation are simulated, and the numerical results of the multi-fields at different temperatures are obtained and analyzed. The results indicate that: (1) the hydrostatic stress gradient is the fundamental factor to activate the hydrogen-induced multi-field coupling behavior excluding the temperature gradient; (2) in the local crack-tip region, hydrides will precipitate faster at the considered higher temperatures, which can be fundamentally attributed to the sensitivity of TSSP and hydrogen diffusion coefficient to temperature. The mechanism is partly explained for the enlarged velocity values of delayed hydride cracking (DHC) at high temperatures before crack arrest. This work lays a foundation for the future research on DHC.


## 1. Introduction

Zircaloy is widely used as nuclear fuel cladding materials due to its high strength, high corrosion resistance and low neutron absorption cross section [1]. In the irradiation environments of pressurized water reactors (PWR) and boiling water reactors (BWR), a fraction of hydrogen atoms, generated by the reaction of zirconium with water, can be absorbed by cladding tubes at the coolant/cladding interface. These hydrogen atoms diffuse under the gradients of temperature, hydrostatic stress and concentration [2] in cladding tubes. When the total concentration of hydrogen exceeds the terminal solid solubility (TSS), the excessive amounts of hydrogen will precipitate as hydrides [3], leading to heat generation and 15%–20% volumetric expansion [4]. Moreover, hardening effect will be induced by hydride precipitation, and the original fracture toughness of Zircaloy will be severely degraded [5], called hydride embrittlement. Especially for the cladding tubes with cracks, the hydrogen atoms tend to diffuse towards the crack-tip region under the hydrostatic stress gradient. Consequently, delayed hydride cracking (DHC) occurs [4,6], which has been listed as one of the main failure mechanisms of Zircaloy components [7].

DHC involves several coupled processes, namely, (i) hydrogen diffusion, (ii) hydride precipitation, (iii) non-mechanical energy flow and (iv) mechanical deformation. The concerned physical fields include the concentration of hydrogen in solid solution, the hydride volume fraction, temperature, displacement, stress and strain et al. They are coupled with each other. The governing equations for the concentration field of hydrogen in solid solution are related to the fields of stress, temperature and hydride volume fraction [8]. TSS of hydrogen in Zircaloy is influenced by temperature and stress [9]. As a result, the concentration field of hydrogen in solid solution is coupled with hydride volume fraction, depending on the temperature and stress fields simultaneously. Furthermore, the temperature field is affected by the variation rate of hydride volume fraction due to exothermic progress of hydride precipitation [9]. And the mechanical fields are also determined by the other fields, because hydrogen dissolution, hydride precipitation and temperature change will lead to eigenstrains, and the mechanical constitutive relations are temperature-dependent [1]. It should be mentioned that Zircaloy experiences irradiation

* Corresponding author.
*E-mail address:* dingshurong@fudan.edu.cn (S. Ding).

https://doi.org/10.1016/j.net.2018.09.014

hardening effect in the demanding in-pile environments, which will also influence the hydrogen-induced multi-field coupling behavior.

For prediction of the structural integrity of Zircaloy components during the in-pile service and the storage stage of spent fuels, experimental and theoretical researches on DHC have been continually carried out since 1960s [10–22]. However, the irradiation effects including irradiation hardening and embrittlement [6,8,23–28] were seldom involved. So far, great improvements have been made in the aspect of theoretical researches. G.P. Marino and J. Freund [29,30] simulated the processes of hydrogen diffusion and hydride precipitation under the temperature gradient, while the hydrostatic stress gradient was not taken into account. Sofronics and McMeeking [31] obtained the coupling behavior of hydrogen transport and mechanical deformation by using an elastic-plastic plane strain model, where the mechanical property variation induced by hydride precipitation was not involved. Lufrano et al. [32–35] calculated the coupling behavior of hydrogen diffusion, hydride precipitation and mechanical deformation under a constant temperature condition, with an elastic-plastic plane strain model adopted; however, the temperature-gradient contribution was excluded.

Comprehensive studies were conducted by Varis and Massih [36–38]. In their publications [36,37], the differential governing equations for hydrogen-induced multi-fields were obtained with thermodynamics theory. The theoretical models for temperature field cover the effects of the transport heat of hydrogen and the exothermic reaction of hydride precipitation. The transient governing equations for hydrogen concentration and hydride volume fraction were developed, and an explicit computational method was proposed. With their developed explicit method, the solid-soluted hydrogen concentration field was not fully coupled with the field of hydride volume fraction in a time increment. Besides, plastic deformation was not considered and the precipitated hydrides were assumed to be isotropic. In fact, δ-hydride appears as a platelet with anisotropic misfit strains.

In some other works [39–41] the hydride reorientation was predicted by phase field modeling. Recently, L.O. Jernkvist and A.R. Massih [4,23] have established more integrated theoretical models. In their studies, the hydride reorientation was involved, and several deformation contributions were introduced into the mechanical constitutive relation, including thermal expansion, the eigen-strains induced by hydrogen dissolution and hydride precipitation, creep and elastic-plastic deformations. Above all, a fully-coupled implicit algorithm was adopted. However, in their modeling the stress contribution to TSS was not reflected, and the temperature field was not calculated and was regarded as a known field.

It is noted that the numerical simulation research is limited with the irradiation hardening effects and hydride-precipitation-induced hardening effects involved in the mechanical constitutive relation. Further study should be performed because these effects will affect the stress states in Zircaloy tubes, and finally change the hydrogen-induced multi-field coupling behavior. Besides, the three-dimensional finite element models for the actual cladding tubes should be adopted, rather than the two-dimensional plate models used in almost all the previous works.

In this study, the differential governing equations for the coupled hydrogen-induced multi-fields are integrated, and a multi-field coupling computation method is developed. In the three-dimensional constitutive relation, the following effects are involved, including the irradiation hardening effects, hydride-precipitation-induced hardening effect and anisotropic misfit strains. The stress update algorithm and consistent stiffness modulus are similarly obtained as Ref. [42]. With self-written subroutines, the three-dimensional numerical simulation of the hydrogen-induced multi-field coupling behavior is realized, and the simulation results for the cracked cladding tubes are obtained and analyzed.

## 2. Multi-field governing equations and the coupling computational method

In this section, the governing equations for the hydrogen-induced multi-fields are given respectively, including the concentration field of solid-soluted hydrogen, the field of hydride volume fraction, the temperature field and displacement, stress, strain fields under the irradiation conditions.

### 2.1. Governing equations for hydrogen diffusion and hydride precipitation

As mentioned above, hydrogen in Zirconium-based alloys exists in two forms: dissolved in the Zircaloy crystal lattice and located in hydrides. Therefore, the total concentration of hydrogen $C^{HT}$ can be given as [37].

$$C^{HT} = fC^{H,hr} + (1-f)C^{H} \tag{1}$$

where $f$ is the hydride volume fraction; $C^{H}$ is defined as the concentration of solid-soluted hydrogen in the volumetric domain $(1-f)V$; $C^{H,hr}$, which can be considered as a constant, represents the concentration of hydrogen in the hydride-occupied volumetric domain $fV$.

Besides, the total concentration of hydrogen is governed by

$$\frac{dC^{HT}}{dt} = -\nabla\cdot J^{H} \tag{2}$$

where $J^{H}$ depicts the hydrogen flux driven by the temperature gradient $\nabla T$, the hydrostatic stress gradient $\nabla\sigma_{mm}$ and the concentration gradient of solid-soluted hydrogen $\nabla C^{H}$. The hydrogen flux is expressed as [37].

$$J^{H} = -(1-f)D^{H}\left[\nabla C^{H} - \frac{\overline{V}^{H}C^{H}}{3RT}\nabla\sigma_{mm} + C^{H}\left(\frac{Q^{H}}{RT^{2}}\right)\nabla T\right] \tag{3}$$

where $R$ is the gas constant; $D^{H}$, $Q^{H}$ and $\overline{V}^{H}$ are the diffusion coefficient, the transport heat of solid-soluted hydrogen and the partial molar volume of hydrogen, respectively. $\frac{\sigma_{mm}}{3}$ denotes the hydrostatic stress.

$$\begin{aligned}&\frac{d\left[fC^{H,hr} + (1-f)C^{H}\right]}{dt}\\ &= \nabla\cdot\left[(1-f)D^{H}\nabla C^{H} - (1-f)\frac{D^{H}\overline{V}^{H}C^{H}}{3RT}\nabla\sigma_{mm} + (1-f)D^{H}C^{H}\left(\frac{Q^{H}}{RT^{2}}\right)\nabla T\right]\end{aligned} \tag{4}$$

According to Eqs. (1)–(3), we have
which represents the transient governing equation of solid-soluted hydrogen concentration fieldcoupled with the field of hydride volume fraction, the temperature field and the hydrostatic stress field. To obtain the definite solutions, the initial conditions and the boundary conditions are given as

$$\begin{cases} C^H = C_0^H & \text{at } t = 0 \\ f = f_0 \end{cases} \tag{5}$$

$$\begin{aligned} J_l^H n_l &= \phi^H \quad \text{on } S_\phi \\ C^H &= C_\psi^H \quad \text{on } S_\psi \end{aligned} \tag{6}$$

where $C_0^H$ and $f_0$ are the initial concentration of solid-soluted hydrogen and the initial hydride volume fraction; $\phi^H$ describes the specified value of hydrogen flux along the external normal of cladding surface $S_\phi$; $C_\psi^H$ represents the specified concentration value of solid-soluted hydrogen at the cladding surface $S_\psi$.

### 2.2. TSSP of hydrogen

To obtain the coupled fields of solid-soluted hydrogen concentration and hydride volume fraction, the terminal solid solubility of hydrogen in Zircaloy should be given. It depends on the temperature loading history [43], having different values of TSSP and TSSD respectively. TSSP represents the TSS value with the current temperature approached from cooling, and TSSD describes the TSS value with the test temperature approached from heating. In this study, TSSP is adopted, because the numerical examples in Section 3 are chosen to have lower temperatures than the in-pile ones of cladding tubes.

For the anisotropic δ-hydride, TSSP is given as

$$C^{TS} = C_e^{TS} \exp\left[\frac{\sigma_{mm} \cdot \overline{V}_H}{3RT} - \frac{\sigma_{ij}\varepsilon_{ij}^{hr}\overline{V}^{hr}}{xRT}\right] \tag{7}$$

where $C_e^{TS}$ is TSSP under stress-free conditions [38], which is temperature-dependent; $\sigma_{ij}$ denotes the stress components; $\varepsilon_{ij}^{hr}$ represents the misfit-strain components due to hydride precipitation; $\overline{V}^{hr}$ denotes the molar volume of hydride; $x$ is the hydrogen atom number in δ-hydride ($ZrH_x$).

Fig. 1 gives the curve of $C_e^{TS}$ vs. temperature. One can see that it is very small at the room temperature and will increase remarkably with temperature.

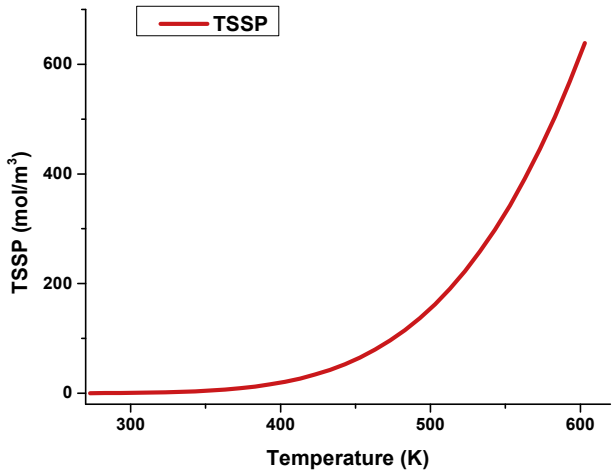


**Fig. 1.** The relation between stress-free TSSP and temperature.

### 2.3. Governing equations for temperature field

With consideration of heat generated during hydride precipitation, the temperature field in the cladding is governed by

$$\rho c \frac{dT}{dt} + \frac{\Delta \overline{H}^{hr}}{\overline{V}^{hr}} \frac{df}{dt} = \nabla \cdot (-q) \tag{8}$$

where $\rho$, $c$ are the density and the temperature-dependent specific heat of Zircaloy; $\Delta \overline{H}^{hr}$ is the enthalpy of forming a mole of hydride; $q$ is the heat flux, expressed as

$$q = -k\nabla T \tag{9}$$

where $k$ is the temperature-dependent thermal conductivity of Zircaloy.

Besides, the initial conditions and boundary conditions are presented as

$$T = T_0 \text{ at } t = 0 \tag{10}$$

$$\begin{aligned} T &= T_h \text{ on } S_H \\ -k\frac{\partial T}{\partial x_l} n_l &= \phi^T \text{ on } S_T \\ -k\frac{\partial T}{\partial x_l} n_l &= h\left(T - T_f\right) \text{ on } S_F \end{aligned} \tag{11}$$

where $T_0$ is the initial temperature in the cladding; $\phi^T$ expresses the specified heat flux value along the external normal $n$ of surface $S_T$; $T_h$ is the specified temperature value; $T_f$ depicts the coolant temperature, and $h$ is the heat transfer coefficient.

### 2.4. Governing equations for displacement, stress and strain fields

The geometric equations considering small deformation, the constitutive equations and the equilibrium equations in the volumetric domain of cladding tubes are given as

$$\varepsilon_{ij} = \frac{1}{2}\left(u_{i,j} + u_{j,i}\right) \tag{12}$$

$$\sigma_{ij} = 2G\varepsilon_{ij}^e + \lambda\varepsilon_{ll}^e\delta_{ij} \tag{13}$$

$$\sigma_{ij,j} = 0 \tag{14}$$

where $u_i \sigma_{ij} \varepsilon_{ij}, \varepsilon_{ij}^e$ are the components of displacement, stress, total strain and elastic strain, respectively. $G$ and $\lambda$ are the Lame coefficients, which are related to the elastic modulus $E$ and Poisson's ratio $\nu$. For the precipited hydrides, their elastic coefficients can be different from the ones of Zircaloy, especially for the isotropic hydrides [38]. In Ref. [38], the hydrided Zircaloy was regarded as a composite material, and the effective elastic coefficients were obtained with a generalized self-consistent model. Whereas, δ-hydrides have about the same elastic properties as -Zircaloy [23]. Hence, the same elastic coefficients as Zircaloy are adopted for hydrides in this study.

Besides, the stresses should obey the boundary conditions as

$$\sigma_{ij} n_j = p_i \text{ on } S_\sigma \tag{15}$$

where $n_j$ denotes the external normal of surface $S_\sigma$, in which the surface tractions $p_i$ are known.

In this study, the total strains are assumed to consist of the elastic strains $\varepsilon_{ij}^e$, the plastic strains $\varepsilon_{ij}^p$, the thermal expansion

**Table 1**
Material parameters used in the numerical simulation.

| | |
|---|---|
| $Q^H$ - heat of transport for hydrogen in solid solution [11] | 25100 J/mol |
| $\overline{V}^H$ - partial molar volume of hydrogen [36] | $7\times10^{-7}$m$^3$/mol |
| $\overline{V}^{Zr}$ - molar volume of zircaloy [36] | $14.06\times10^{-6}$m$^3$/mol |
| $\overline{V}^{hr}$ - molar volume of hydride [36] | $16.3\times10^{-6}$m$^3$/mol |
| $x$ ($ZrH_x$) - hydrogen atom number in δ-hydride [36] | 1.66 |
| $\Delta\overline{H}^{hr}$ - enthalpy of formation of a mole of hydride [36] | −63517.41 J/mol |
| $C^{H,hr}$ - concentration of hydrogen in hydrides [36] | $1.02\times10^5$mol/m3 |
| $C_e^{TS}$ - hydrogen terminal solid solubility under stress-free conditions [36] | $6.3741\times10^5\exp(-34542.75/RT)$mol/m$^3$($R$-the gas constant) |
| $D^H$ - diffusion coefficient [36] | $2.17\times10^{-7}\exp(-35087.06/RT)$m$^2$/s |
| $\rho$ - density [37] | 6490 kg/m$^3$ |
| $c$ - specific heat [37] | $226.69+0.206639T$-$6.4925\times10^{-5}T^2$ ($T$ in K) |
| $\alpha$ - thermal expansion coefficient [1] | $5.58\times10^{-6}$ K$^{-1}$ |
| $k$ - thermal conductivity [1] | $7.51+2.09\times10^{-2}T$-$1.45\times10^{-5}T^2$+$7.67\times10^{-9}T^3$ ($T$ in K) |
| $E$ - Young's modulus [1] | $9.8067\times10^4\times(9.9\times10^5$-$566.9(T$-$300))/k_1$($T$ in K) |
| $k_1$ −modifying factor for $E$ [1] | $0.88+0.12\exp(-\varphi t/10^{25})$ ($\varphi t$-fast neutron fluence in n/m$^2$ ) |
| $\nu$ - Poisson's ratio [1] | $0.3303+8.376\times10^{-5}$($T$-300) ($T$ in K) |
| $h$ − convection heat transfer coefficient | $2.0\times10^4$ W/(m$^2$.K) |

strains $\varepsilon_{ij}^T$, the egien-strains $\varepsilon_{ij}^H$ induced by hydride precipitation and hydrogen dissolution. Therefore, the elastic strains can be derived as

$$\varepsilon_{ij}^e=\varepsilon_{ij}-\varepsilon_{ij}^T-\varepsilon_{ij}^H-\varepsilon_{ij}^p \tag{16}$$

The egienstrains due to hydrogen dissolution and hydride precipitation are described as

$$\begin{cases}\varepsilon_{ij}^H=f\varepsilon_{ij}^{hr}+(1-f)\overline{V}^HC^H\big/3\\ \varepsilon_\theta^{hr}=6.646\times10^{-2}+1.9348\times10^{-5}T\\ \varepsilon_r^{hr}=\varepsilon_z^{hr}=3.888\times10^{-2}+2.315\times10^{-5}T\end{cases} \tag{17}$$

The strain-hardening curve with irradiation/hydride-induced hardening effects involved is described as [1].

$$\begin{aligned}\sigma&=K\varepsilon^n\\ K&=K(T)+K(C_{HE})+K(\phi t)\\ n&=n(T)\times n(C_{HE})\times n(\phi t)\end{aligned} \tag{18}$$

where $C_{HE}$ in PPM is defined as the hydrogen concentration in excess of TSS, that is, $C_{HE}$=$C^{HT}$-$C^{TS}$; $\varphi t$ is the fast neutron fluence in n/m$^2$. $K(T)$, $K(C_{HE})$, $K(\varphi t)$ are the strength coefficients contributed by temperature, $C_{HE}$ and $\varphi t$, respectively. $n(T)$, $n(C_{HE})$, $n(\varphi t)$ are respectively the strain hardening coefficients with respect to temperature, $C_{HE}$ and $\varphi t$. Their expressions are given as

$$\begin{aligned}K(T)&=1.17628\times10^9+T\left[4.5485\times10^5+T\left(-3.2818\times10^3+1.7275T\right)\right]\\ K(C_{HE})&=C_{HE}\left[1.288\times10^6+C_{HE}\left(7.546\times10^3-17.84C_{HE}\right)\right]\\ K(\phi t)&=5.54\times10^{-18}\phi t\end{aligned} \tag{19}$$

and

$$\begin{aligned}n(T)&=-9.49\times10^{-2}+T\left[1.165\times10^{-3}+T\left(-1.992\times10^{-6}+9.588\times10^{-10}T\right)\right]\\ n(C_{HE})&=1+2.298\times10^{-3}C_{HE}+4.138\times10^{-6}C_{HE}^2-1.5\times10^{-8}C_{HE}^3\\ n(\phi t)&=1.369+0.032\times10^{-25}\phi t\end{aligned} \tag{20}$$

It turns out to become a nonlinear problem to solve the mechanical fields, when the plastic strains are considered. As a result, the three-dimensional stress update algorithms and consistent tangent stiffness should be derived out to deal with the complex plastic behavior.

The contained material parameters in the governing equations of Sections 2.1–2.4 are listed in Table 1.

### 2.5. Multi-field coupling computational method

To solve the above hydrogen-induced multi-field coupling problem, a sequentially coupled analysis method is put forward. As presented in Fig. 2, the whole numerical calculation is divided into a number of time increments.

For a typical time increment $[t, t+\Delta t]$, the temperature field is firstly obtained through iterative computation, in which the variation rates of hydride volume fraction from the previous incremental calculation are adopted, this means that $\frac{df}{dt}\approx\frac{f^t-f^{t-\Delta t}}{\Delta t}$. Then, with the node temperature results introduced, the displacement field can be worked out with the N-R iterative method. It is noted that the increments of solid-soluted hydrogen concentration and hydride volume fraction from the previous incremental calculation are used. When the displacement increments are converged, the stresses and strains at the integration points can be acquired simultaneously. Afterwards, based on the results for the integration points, the concerned

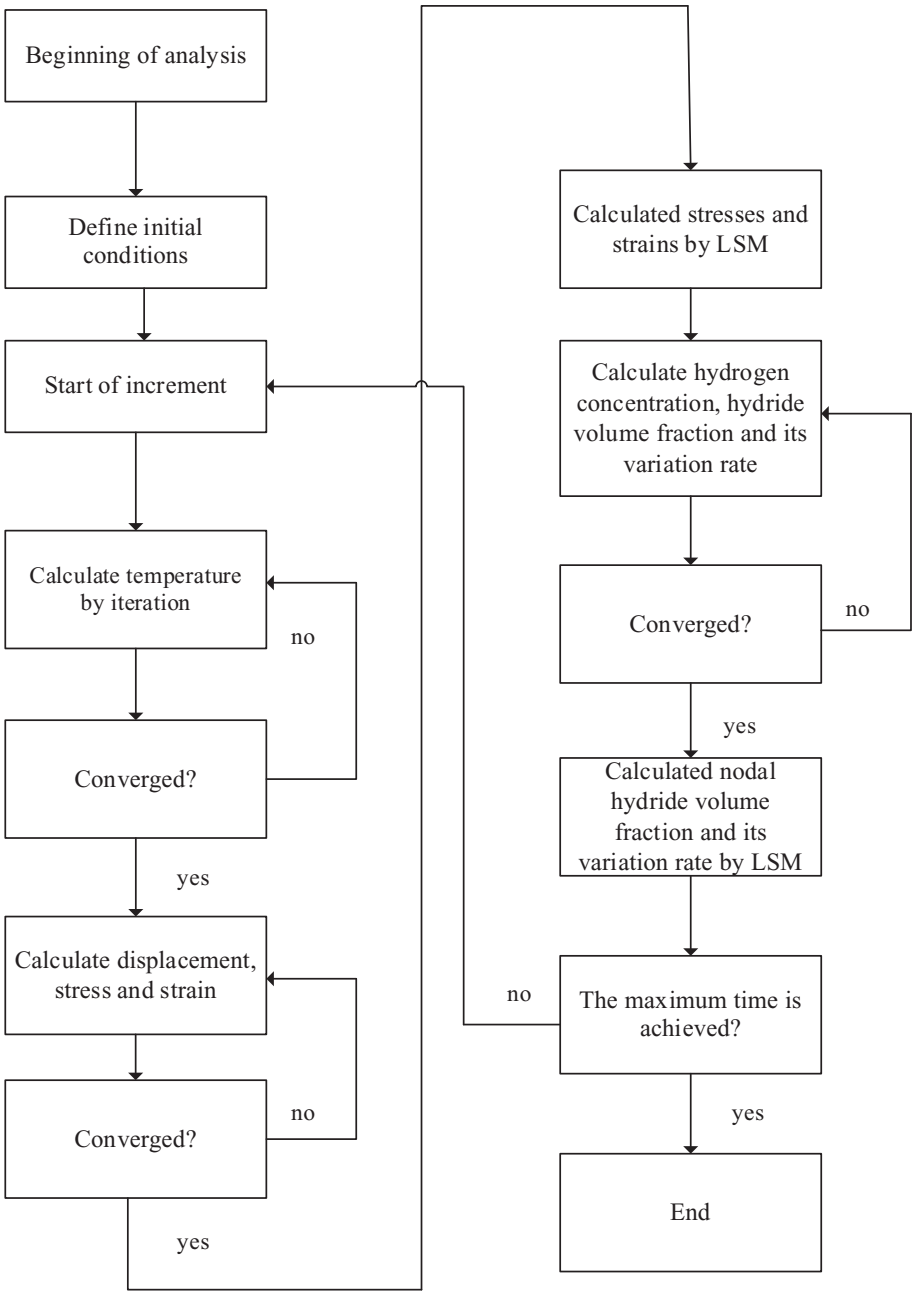


**Fig. 2.** Calculation flowchart of the multi-field coupling problem.

strain/stress components and the hydrostatic stresses for the element nodes are computed by least square method (LSM). Subsequently, the concentration field of solid-soluted hydrogen is iteratively calculated, which is coupled with the hydride volume fraction at the integration points. Ultimately, the field of hydride volume fraction and its variation rate are obtained by LSM. If the maximum time is not achieved, the next incremental calculation begins.

In accordance with the developed multi-field coupling computational method together with the corresponding equivalent integral forms and finite element equations for every field, the special subroutines have been self-written and verified.

## 3. Results and discussions for the hydrogen-induced multi-field coupling behavior in a cracked cladding tube

### 3.1. Finite element model

As shown in Fig. 3(a), it is assumed that the cladding tube has two long axial cracks, and its normal displacement components at the two ends are zero. The cladding tube is subjected to uniform pressures. Before applying internal pressures, the total hydrogen concentration is uniform within the cladding tube, which is equal to the stress-free TSSP at 473 K. Thus, according to the symmetry of loads and geometry, a quarter of the cladding tube slice is set as the

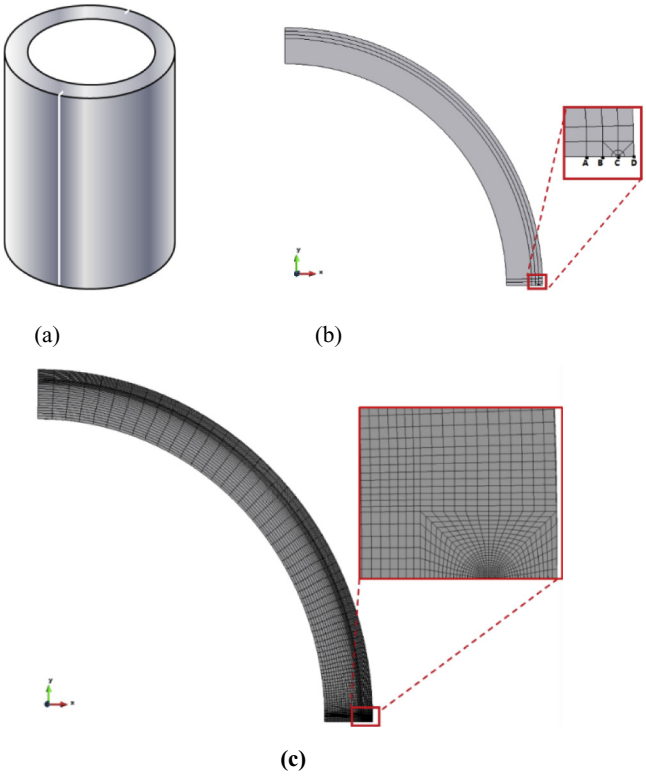


**Fig. 3.** (a) A cladding tube with two axial cracks, (b) the finite element model and the output path and (c) the finite element meshes.

finite element model, as illustrated in Fig. 3(b). The crack deepness is 0.07 mm (CD in Fig. 3(b)). The inner and outer radii of the cladding tube are 4.3 mm and 5 mm, respectively.

It is noted that the hydrogen diffusion coefficient and TSSP are sensitive to temperature. In order to investigate the effects of temperature on the hydrogen-induced multi-field coupling behavior, three out-pile experiments at different temperatures are simulated, as given in Table 2. In the storage stage of spent fuels, the cladding temperature will gradually decrease from high in-pile temperatures. So, the three temperature cases are selected in Table 2. Through the out-pile experiments, the DHC velocities can be obtained at different temperatures [44]. The actual multi-field coupling processes and detailed mechanism are hard to be examined in the experiments, and three-dimensional numerical simulation research can be helpful.

Owing to the fact that hydrides will precipitate when the total hydrogen concentration exceeds its terminal solid solubility, so the initial hydride volume fractions for Case B and Case C are not zero. The initial hydride volume fraction for Case C is the highest, due to existence of the lowest TSS. The internal pressures $p$ for the three cases all increase linearly with time, and eventually reach 30 MPa after 30 s and then remain unchanged. The fast neutron fluence is set as $2 \times 10^{25} \mathrm{n/m^2}$. The total computation time is 500s, and the time increment for every step is set as 5s.

The finite element meshes are depicted in Fig. 3(c), and it can be found that the mesh is refined around the crack tip. The model is discretized into 6624 elements with the 8-node hexahedral element. It is confirmed that enough computational precision can be achieved.

### 3.2. General analysis of the hydrogen-induced multi-field coupling results

Through three-dimensional numerical simulation, the hydrogen-induced multi-field coupling results are obtained at different time instants. Fig. 4 (a), (b) and (c) present the contour plots of hydrostatic stress, solid-soluted hydrogen concentration and hydride volume fraction at $500^{\mathrm{th}}$ second for case A, respectively.

It can be clearly seen from Fig. 4 (a) that stress concentration appears at the crack tip. In the vicinity of crack tip, the hydrostatic stresses have a big difference. On the left side of crack tip, the hydrostatic stresses are very large positive ones. As a whole, on the right side of crack tip, the stresses are much smaller and negative magnitudes can be found. A high gradient of hydrostatic stress forms from the right side to the left side of crack tip. According to Eq. (3), it can be predicted that the hydrogen atoms will diffuse from the right to the left of crack tip, driven by a high gradient of hydrostatic stress. Of course, all the hydrogen atoms surrounding the crack tip will tend to diffuse towards the crack front, and then precipitate as hydrides.

In Fig. 4 (b), one can find that at the region far away from the crack tip the solid-soluted hydrogen concentration in $\mathrm{mol/mm^3}$ is close to the stress-free TSSP. From the magnified figure, one can see that around the crack tip there are two areas with low concentration of solid-soluted hydrogen. Comparing the contour plots in Fig. 4 (a) and (b), one can observe that the left blue area has very large positive hydrostatic stresses, and the right blue area has very small hydrostatic stresses. It can be predicted that in the left area the small concentration of solid-soluted hydrogen equals to the lowered TSSP there, which results from large tensile stresses. In the right area, the current smaller hydrogen concentration is possible to be caused by the fact that the original hydrogen atoms move to the left area. Simultaneously, it can be known from Eq. (3) that the existent concentration gradient of solid-soluted hydrogen will also drive the hydrogen atoms to diffuse towards the crack tip. Of course, it is understandable that the formed concentration gradient here mainly stems from the existence of stress gradients.

One can obtain from Fig. 4 (c) that hydride precipitation only occurs in the local crack-tip region. And the area with hydride precipitation corresponds to the one with the smallest concentration of solid-soluted hydrogen in Fig. 4 (b). So, the concentration of

**Table 2**
Initial and boundary conditions for the cladding tube.

| | The initial conditions | | | Boundary conditions | |
|---|---|---|---|---|---|
| | Concentration of hydrogen in solid solution ($\mathrm{mol/m^3}$) | Hydride volume fraction ($10^{-4}$) | Total concentration of hydrogen ($\mathrm{mol/m^3}$) | Inside the cladding tube | Outside the cladding tube |
| Case A | 97.641 | 0 | 97.641 | $T = 473\mathrm{K}$, $p$ | $T = 473\mathrm{K}$ |
| Case B | 9.2662 | 8.6650 | 97.641 | $T = 373\mathrm{K}$, $p$ | $T = 373\mathrm{K}$ |
| Case C | 0.6163 | 9.5123 | 97.641 | $T = 300\mathrm{K}$, $p$ | $T = 300\mathrm{K}$ |

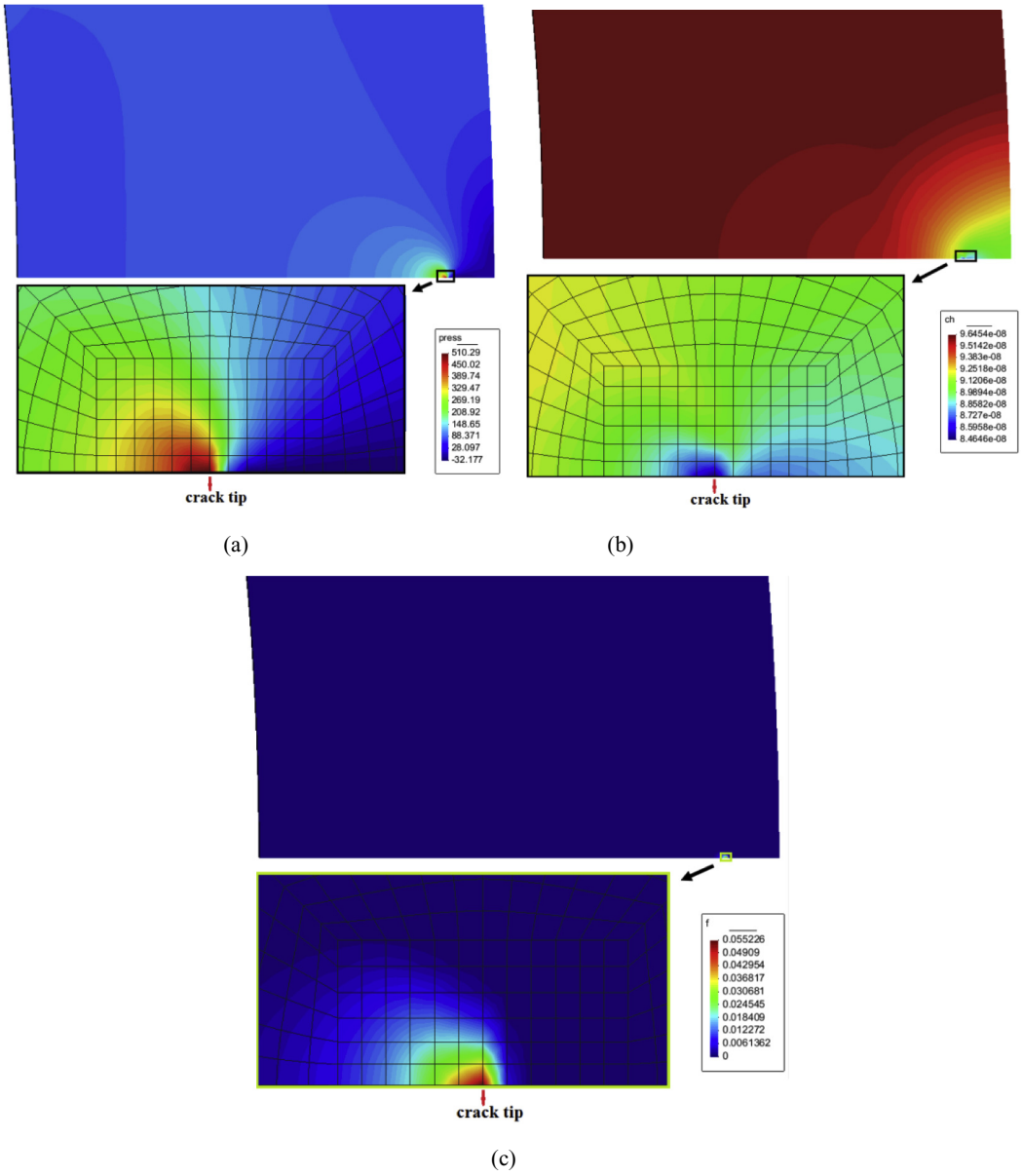


**Fig. 4.** Contour plots of (a) hydrostatic stress, (b) solid-soluted hydrogen concentration and (c) hydride volume fraction (c) at 500$^{th}$ second for case A.

solid-soluted hydrogen in that area equals to TSSP there. The first dark blue area in front of the crack tip in Fig. 4 (b) actually means that low TSSP exists there. And one can also find that hydride precipitation appears mainly in the left side of the crack tip. On one hand, it results from lower TSSP values there. On the other hand, the hydrostatic stress gradient tends to drive the hydrogen atoms to diffuse towards this local area. This analysis is consistent with the previous explanation and predictions.

In Fig. 4 (a)-(c), the hydrogen-induced multi-field coupling behavior for Case A is briefly described. In fact, the basic coupling mechanism is similar for Case B and Case C. Owing to the sensitivities of stress-free TSSP and hydrogen diffusion coefficient to temperatures, the distribution and evolution laws of hydrogen-induced multi-fields for the three cases differ from each other. From the contour plots in Fig. 4, it can be observed that the maximum magnitudes of hydrostatic stress, solid-soluted hydrogen and hydride volume fraction all locate at the cracking plane. Thus, in the next three sections, the multi-field results at different instants for the three cases will be given along the path of DCBA in Fig. 3(b), and the effects of temperature will be analyzed.

### 3.3. *Effects of temperature on the hydrostatic stress results*

Fig. 5 (a), (b) and (c) exhibit the hydrostatic stresses along the radial path at different time for the considered three cases. Stress concentration can be clearly found at the crack tip, and in fact in the radial path both the hoop and radial stresses are the largest at the crack tip. From Fig. 5 (a), one can see that the hydrostatic stresses at the near-tip region decrease with time, and from 100s to 500s the hydrostatic stress at the crack tip reduces by ~37.5%. With increasing time, the hydrostatic stress gradient is also lowered. However, the hydrostatic stresses vary differently with time for the other two cases. As shown in Fig. 5 (b), a decreasing trend with time can be noticed, but the stresses at different instants change slightly. As illustrated in Fig. 5 (c), the hydrostatic stresses hardly vary with time. From Fig. 5 (d), one can observe that at the crack tip the

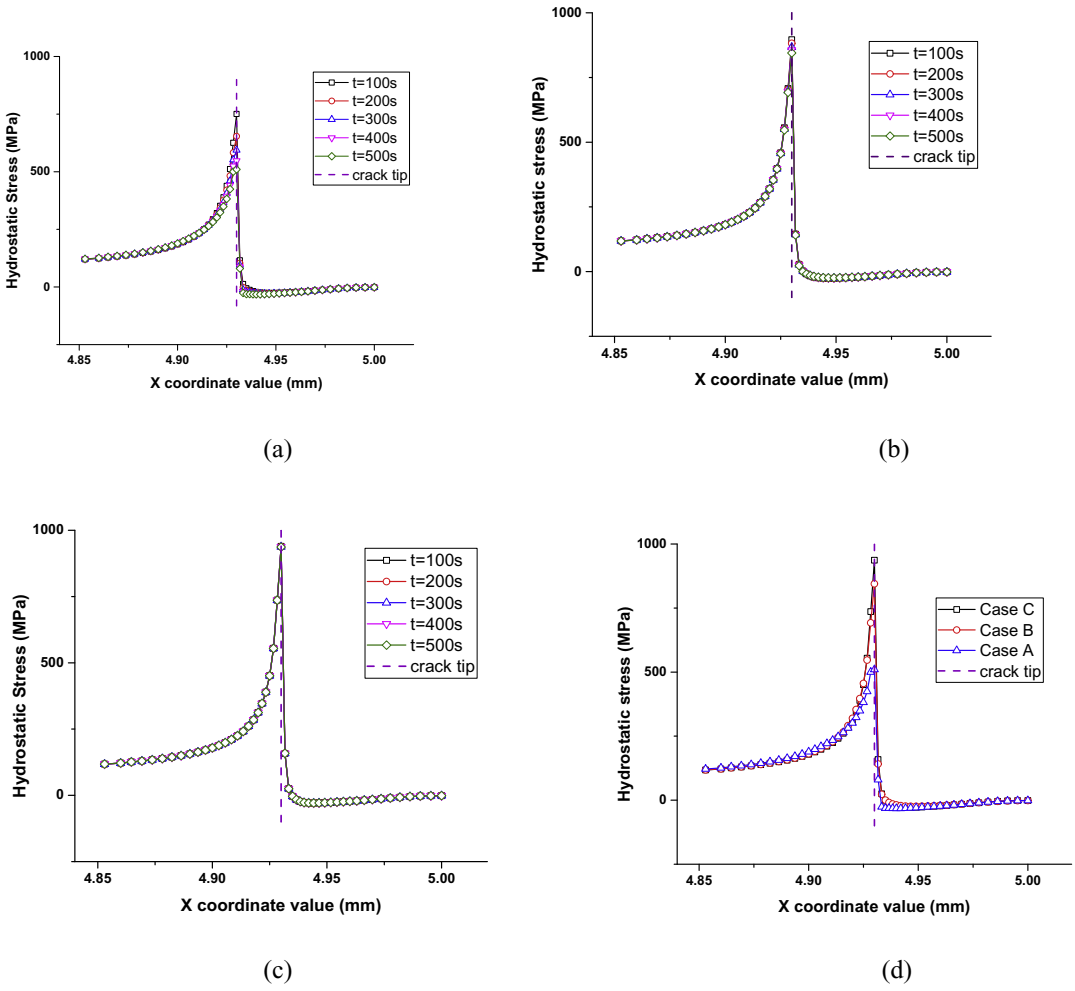


**Fig. 5.** Hydrostatic stresses for (a) Case A, (b) Case B, (c) Case C (c) and (d) the results at the end of 500s for the three cases along the radial path on the crack plane.

hydrostatic stresses at the end of 500s will be much lower for Case A, and the difference between Case A and Case C becomes larger than that at 100$^{th}$ second. One can also find that there is a very large gradient of hydrostatic stress on the right of crack tip, which will drive the hydrogen atoms to move from the right to the left.

It can be obtained that the temperature has an important effect on the hydrostatic stresses. At the instant after loading, the differences attribute to the temperature dependence of elasto-plasticity properties. It is known that the elastic modulus will decrease with temperature, and especially the yield strength will be much lower at higher temperatures. With increase of time, the different evolution laws will be related to the processes of hydrogen diffusion and hydride precipitation, and the effects of temperature on the solid-soluted hydrogen concentration and hydride volume fraction will be discussed in the following sections.

### *3.4. Effects of temperature on the solid-soluted hydrogen concentration*

For the three cases, the solid-soluted hydrogen concentration along the radial path at different time can be found in Fig. 6. It is noted that the concentration at the crack tip is the lowest, which is induced by the occurrence of stress concentration at the crack tip. It is known from Eq. (7) that large tensile stresses at the crack tip will result in low TSSP. Hydride precipitation all appears in the local crack-tip area for the three cases (see Fig. 7), so the solid-soluted hydrogen concentration at the crack tip is the same as TSSP there. Compared to the stress-free magnitudes, TSSP at the crack tip decreases by ~20% at 100$^{th}$ second for Case A, and TSSP for Case B decreases by ~26.7% at the crack tip, and for Case C it decreases by ~30.5%. Owing to the fact that the tensile stresses at the crack tip are larger at lower temperatures, the relative variation of TSSP at the crack tip appears to be higher for Case C. So, it can be obtained that the stress-dependence of TSS should be considered for a stress concentration problem. The stress-dependence of TSSP results in the concentration gradient of solid-soluted hydrogen in the local region of crack tip. One can know from Eq. (3) that the hydrogen diffusion direction is opposite to that of hydrogen concentration gradient, and the same to that of hydrostatic stress gradient. As a result, both of the gradients will drive the hydrogen atoms to move towards the crack tip from the neighborhood, and the hydride volume fraction will be locally heightened.

On the right side of the crack tip, i.e. CD in Fig. 3 (b), the hydrogen atoms diffuse towards the crack tip and its hydrogen concentration decreases with time, as can be seen from Fig. 6(a) and (b). One can also see that the decreasing rate of solid-soluted hydrogen concentration is getting lower and lower. As for the hydrogen concentration results at the temperature of 300 K, one can see from Fig. 6 (c) that no evident variation undergoes. These distribution and evolution phenomena are closely related to those of hydrostatic stress and hydride volume fraction, which will be analyzed in the next section.

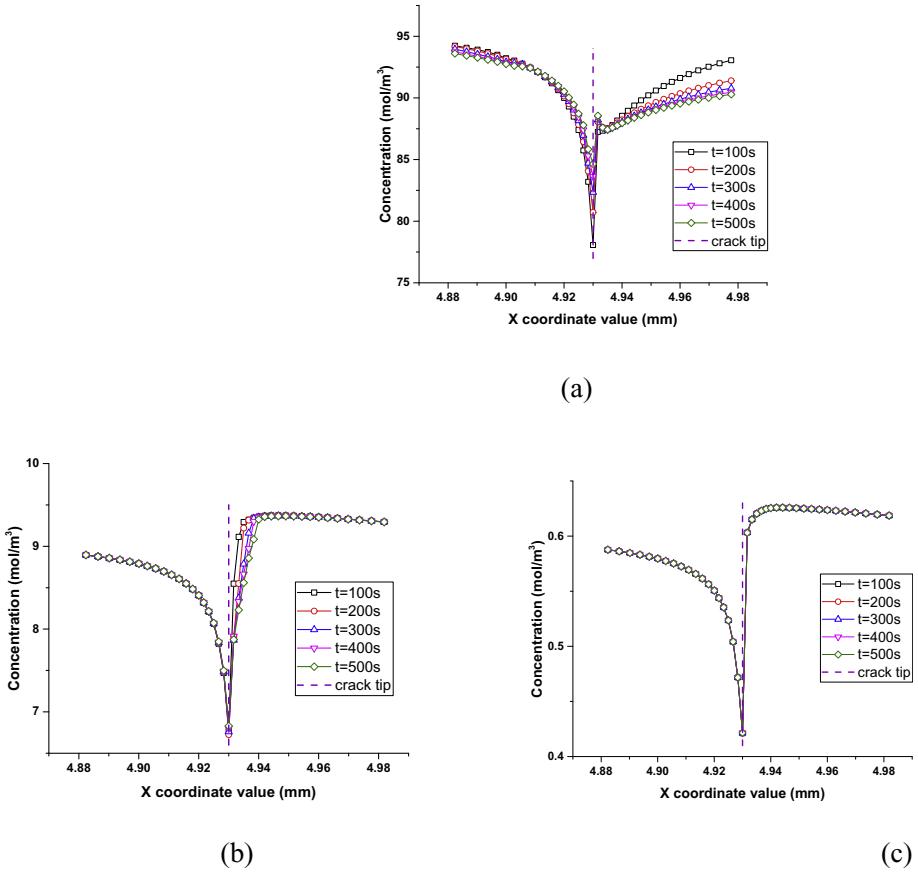


**Fig. 6.** Concentration results of hydrogen in solid solution for (a) Case A, (b) Case B and (c) Case C along the radial path on the crack plane.

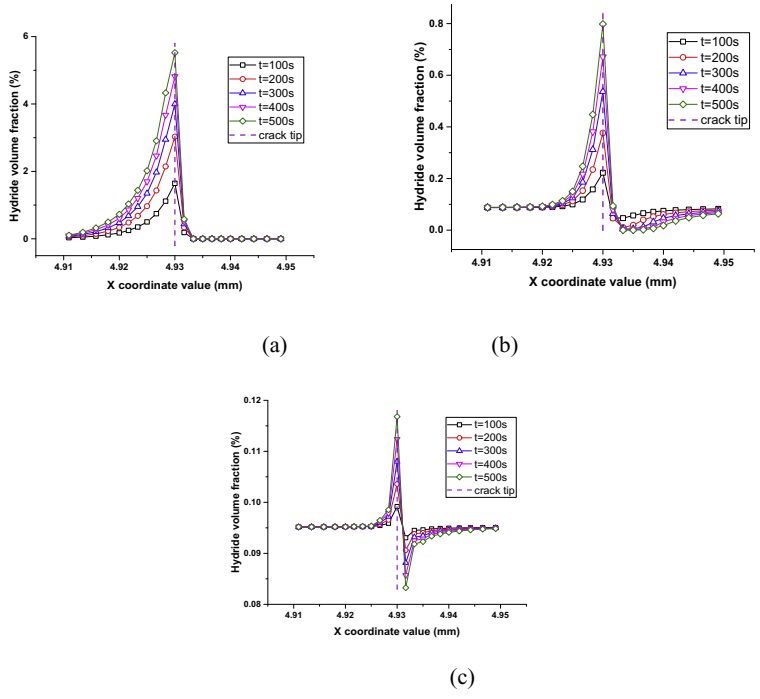


**Fig. 7.** Hydride volume fraction results for (a) Case A, (b) Case B and (c) Case C along the radial path on the crack plane.

### 3.5. Effects of temperature on the hydride volume fraction

The hydride volume fraction for Case A is shown in Fig. 7(a). One can see that hydride precipitation mainly occurs on the left side of the crack tip. At the 500$^{th}$ second, the hydride volume fraction reaches ~6%. In a very small region on the right side of crack tip, there exist hydrides whose volume fraction increases slightly with time. As analyzed in Sections 3.3 and 3.4, the hydrogen atoms prefer to diffuse towards the crack tip. Due to existence of large tensile stresses in the local crack-tip region, TSSP values become lower than those in the other regions. Hence, it is easier for hydride precipitation at the crack tip. With the rise of the hydride volume fraction, the induced misfit strains also increase. Accordingly, the local area will be compressed. Thus, one can observe from Figs. 6(a) and 7(a), the hydrostatic stress lowers and the solid-soluted hydrogen concentration enlarges. And both gradients are lowered and the corresponding variation rates decreases. Thus, it can be found that the precipitation velocity of hydrides decreases with time. Besides, it can be known from Eq. (3) that the effective hydrogen diffusion coefficient $(1-f)D$ will decline with hydride volume fraction. While, on the right side of crack, the hydride volume fraction is much smaller, the effective hydrogen diffusion coefficient will be higher. Consequently, the hydrogen atoms here will diffuse more quickly towards the crack tip. Thus, one can find from Fig. 7 (a) that the solid-soluted hydrogen concentration decreases largely there from 100s to 500s.

The results for Case B and Case C are presented in Fig. 7(b) and (c). Different from Case A, hydrides already exist before applying the internal pressure. Driven by the hydrostatic stress gradient and solid-soluted hydrogen concentration gradient, it is similar that the hydride volume fraction increases over time on the left side of crack tip. However, compared to the results in Fig. 7 (a), it can be found that the occupied areas by hydrides are smaller and the achieved maximum values are much lower than that for Case A. So, the hydrostatic stresses around the crack tip changes slightly and slowly for Case B and Case C. One can also find an interesting phenomenon that on the right side of crack tip a part of original hydrides dissolve, and in some areas the hydride volume fraction becomes zero, as depicted in Fig. 7(b) and (c). And on the left side of crack tip, the hydride volume fraction remains unchanged at a distance away from the crack tip. It can be predicted that hydride precipitation on the left side of crack tip will be accelerated for Case A if original hydrides exists in the cladding tubes.

At lower temperatures, the stress-free TSSP can be very low. As listed in Table 2, its value at 473 K is more than 10 times of that at 373 K and more than 100 times of that at 300 K. So the amount of movable hydrogen atoms for Case B and Case C are much smaller than that for Case A, as well as the corresponding hydrogen concentration gradients. On the other hand, the hydrogen diffusion coefficient is also sensitive to temperature, and its value at 473 K is almost 11 times of that at 373 K, and 172 times of that at 300 K. So, it is understandable that the hydride volume fractions in the crack-tip region for Case B and Case C are much lower than that for Case A, even though their hydrostatic stress gradients are higher. The detailed mechanism can be obtained from Eq. (3). As temperature gradient is not considered here, the total hydrogen flux is only affected by the first two terms. It is worth noting that the term with hydrostatic stress gradient is also affected by the solid-soluted hydrogen concentration, which is equal to TSSP in the crack-tip region. So, in addition to the contributions of solid-soluted hydrogen concentration gradient and hydrostatic stress gradient, TSSP has an important effect on hydride precipitation. As given in Fig. 8, the hydride volume fraction at 373 K and 300 K is higher at first, but the velocity of hydride precipitation is much higher for Case A.

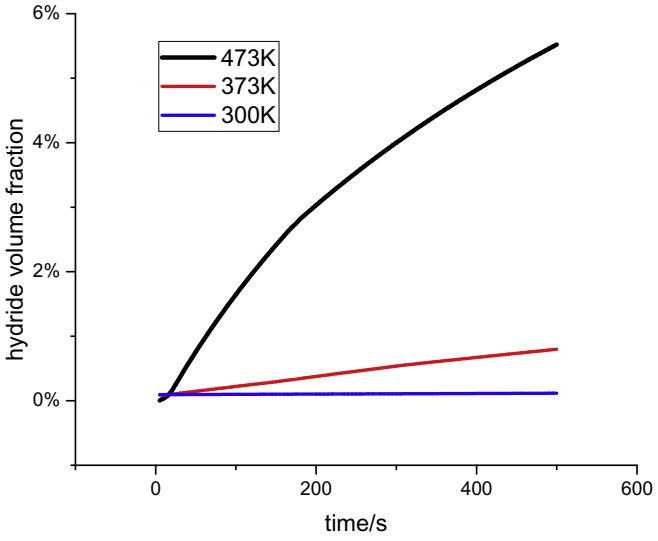


**Fig. 8.** Evolution results of hydride volume fraction at the crack tip at different temperatures.

One of the important effects of hydride precipitation is that it can heavily degrade the fracture toughness of Zircaloy, so it can be obtained that the structural integrity will be threatened for a cracked cladding tube subjected to internal pressures at comparably high temperatures. This conclusion agrees with the experimental results that the DHC velocity will increase with temperature in a certain temperature range. But if the temperature is much higher than 473 K, the threat caused by hydride precipitation may decrease [44], which may be due to the much higher toughness and much lower yield strength. As mentioned previously, excluding the effect of temperature gradient, the basic mechanism of hydrogen diffusion stems from enough high hydrostatic stress gradients. If the yield strength is very low, the necessary conditions for fracture are hard to be met.

## 4. Conclusions

In this study, the differential governing equations for hydrogen diffusion-hydride precipitation and mechanical deformation are given. In the mechanical constitutive relation, the contributions of thermal expansion, the eigenstrains induced by hydrogen dissolution and hydride precipitation, irradiation- and hydride-induced hardening plasticity are involved. A multi-field coupling computational method is put forward. The three-dimensional numerical simulation of the hydrogen-induced multi-field coupling behavior is implemented for the cracked Zircaloy cladding tubes, and the obtained results are analyzed. The conclusions are drawn as:

(1) Hydrides will only precipitate at the local crack-tip area, and the hydride volume fraction in front of the crack tip will increase with time. As a whole, a large quantity of hydrogen atoms can be found to diffuse along the cracking direction from the back side to the front side of crack tip.
(2) Excluding the temperature gradient, the hydrostatic stress gradient is the fundamental factor to result in the hydrogen-induced multi-field coupling behavior in the cracked Zircaloy cladding tubes. It will induce a lower TSSP in the crack-tip region, and the concentration of solid-soluted hydrogen will accordingly form. Both gradients drive hydrogen diffusion.

(3) In a cladding tube with cracks, hydride precipitation at higher temperature will be much quicker than that at lower temperature, which can be fundamentally attributed to the sensitivity of TSSP and hydrogen diffusion coefficient to temperature.

In this study, the damage and cracking process are not considered, with them involved the multi-field coupling results will be affected because of the varied stress field. This study lays a foundation for the future research work.

## Acknowledgements

The authors thank for the supports of National Natural Science Foundation of China (No. 11772095, 11572091), the support of the National Key Research and Development Program of China (2016YFB0700103), the support of the foundation from Science and Technology on Reactor System Design Technology Laboratory.

## References

[1] L.J. Siefken, E.W. Coryell, E.A. Harvego, et al., MATPRO–A Library of Materials Properties for Light-water-reactor Accident Analysis. Idaho Falls, Idaho National Engineering and Environmental Laboratory, 2001.
[2] P. Shewmon, Diffusion in Solids. The Minerals, Metals & Materials Society, Diffusion in Solids, second ed., Retroactive Coverage, United States), 1989, p. 246, 1989.
[3] C.E. Coleman, D. Hardie, The hydrogen embrittlement of α-zirconium—a review, J. Less Common Met. 11 (3) (1966) 168–185.
[4] L.O. Jernkvist, A.R. Massih, Multi-field modelling of hydride forming metals. Part I: model formulation and validation, Comput. Mater. Sci. 85 (2014) 363–382.
[5] C.E. Coleman, Cracking of hydride-forming metals and alloys, in: Comprehensive Structural Integrity, 6, 2003, pp. 103–161.
[6] M.P. Puls, The Effect of Hydrogen and Hydrides on the Integrity of Zirconium Alloy Components: Delayed Hydride Cracking, Springer Science & Business Media, 2012.
[7] C.K. Chao, K.C. Yang, C.C. Tseng, Rupture of spent fuel Zircaloy cladding in dry storage due to delayed hydride cracking, Nucl. Eng. Des. 238 (1) (2008) 124–129.
[8] C.L. Briant, Z.F. Wang, N. Chollocoop, Hydrogen embrittlement of commercial purity titanium, Corrosion Sci. 44 (8) (2002) 1875–1888.
[9] A.G. Varias, J.L. Feng, Simulation of hydride-induced steady-state crack growth in metals–Part I: growth near hydrogen chemical equilibrium, Comput. Mech. 34 (5) (2004) 339–356.
[10] S.Q. Shi, M.P. Puls, Dependence of the threshold stress intensity factor on hydrogen concentration during delayed hydride cracking in zirconium alloys, J. Nucl. Mater. 218 (1) (1995) 30–36.
[11] E. Smith, Threshold stress criterion for delayed hydride crack initiation at a blunt notch in zirconium alloys, Int. J. Pres. Ves. Pip. 68 (1) (1996) 53–61.
[12] K.S. Chan, A micromechanical model for predicting hydride embrittlement in nuclear fuel cladding material, J. Nucl. Mater. 227 (3) (1996) 220–236.
[13] K. Une, S. Ishimoto, Y. Etoh, et al., The terminal solid solubility of hydrogen in irradiated Zircaloy-2 and microscopic modeling of hydride behavior, J. Nucl. Mater. 389 (1) (2009) 127–136.
[14] A.T. Motta, L.Q. Chen, Hydride formation in zirconium alloys, JOM (J. Occup. Med.) 64 (12) (2012) 1403–1408.
[15] J.A. Szpunar, W. Qin, H. Li, et al., Roles of texture in controlling oxidation, hydrogen ingress and hydride formation in Zr alloys, J. Nucl. Mater. 427 (1) (2012) 343–349.
[16] C. Sun, J. Tan, et al., Critical temperature of delayed hydride cracking in N-18 Zircaloy, Acta Metall. Sin. 45 (5) (2009) 541–546.
[17] W.J. Zhao, Development of new nuclear cladding in French PWR, Nucl. Power Eng. 21 (3) (2000) 278–284.
[18] Y. Gou, Y. Li, Y. Liu, et al., Evaluation of a delayed hydride cracking in Zr–2.5 Nb CANDU and RBMK pressure tubes, Mater. Des. 30 (4) (2009) 1231–1235.
[19] M.D. Pandey, M. Wang, G.A. Bickel, A probabilistic approach to update lower bound threshold stress intensity factor (K IH) for delayed hydride cracking, Nucl. Eng. Des. 240 (10) (2010) 2682–2690.
[20] A. Zieliński, S. Sobieszczyk, Hydrogen-enhanced degradation and oxide effects in zirconium alloys for nuclear applications, Int. J. Hydrogen Energy 36 (14) (2011) 8619–8629.
[21] M.D. Pandey, D.D. Radford, A statistical approach to the prediction of pressure tube fracture toughness, Nucl. Eng. Des. 238 (12) (2008) 3218–3226.
[22] J.I. Mieza, G.L. Vigna, G. Domizzi, Evaluation of variables affecting crack propagation by Delayed Hydride Cracking in Zr–2.5 Nb with different heat treatments, J. Nucl. Mater. 411 (1) (2011) 150–159.
[23] L.O. Jernkvist, Multi-field modelling of hydride forming metals Part I: model formation and validation, Comput. Mater. Sci. 85 (2014) 383–401.
[24] N. Hashimoto, T.S. Byun, K. Farrell, et al., Deformation microstructure of neutron-irradiated pure polycrystalline metals, J. Nucl. Mater. 329 (2004) 947–952.
[25] E.R. Bradley, G.P. Sabol, Zirconium in the Nuclear Industry: Eleventh International Symposium, ASTM, 1996.
[26] A.M. Garde, G.P. Smith, R.C. Pirek, Effects of Hydride Precipitate Localization and Neutron Fluence on the Ductility of Irradiated Zircaloy-4//Zirconium in the Nuclear Industry: Eleventh International Symposium, ASTM International, 1996.
[27] F. Yunchang, D.A. Koss, The influence of multiaxial states of stress on the hydrogen embrittlement of zirconium alloy sheet, Metall. Trans. A 16 (4) (1985) 675–681.
[28] J.H. Huang, S.P. Huang, Effect of hydrogen contents on the mechanical properties of Zircaloy-4, J. Nucl. Mater. 208 (1) (1994) 166–179.
[29] G.P. Marino, HYDIZ, A 2-dimensonal computer program for migration of interstitial solutes of finite solubility in a thermal gradient (LWBR Development Program), Bettis Atomic Power Lab., Pittsburgh, PA (USA), 1974.
[30] J. Freund, A Model for Thermal Diffusion of Hydrogen in Zirconium Alloys, Helsinki University of Technology, 1992.
[31] P. Sofronis, R.M. McMeeking, Numerical analysis of hydrogen transport near a blunting crack tip, J. Mech. Phys. Solid. 37 (3) (1989) 317–350.
[32] D.R. Metzger, R.G. Sauvé, A Self-induced Stress Model for Simulating Hydride Formation at Flaws, American Society of Mechanical Engineers, New York, NY (United States), 1996.
[33] J. Lufrano, P. Sofronis, Micromechanics of hydride formation and cracking in zirconium alloys, Comput. Model. Eng. Sci. 1 (2) (2000) 119–131.
[34] J. Lufrano, P. Sofronis, H.K. Birnbaum, Elastoplastically accommodated hydride formation and embrittlement, J. Mech. Phys. Solid. 46 (9) (1998) 1497–1520.
[35] J. Lufrano, P. Sofronis, H.K. Birnbaum, Modeling of hydrogen transport and elastically accommodated hydride formation near a crack tip, J. Mech. Phys. Solid. 44 (2) (1996) 179–205.
[36] A.G. Varias, A.R. Massih, Hydride-induced embrittlement and fracture in metals—effect of stress and temperature distribution, J. Mech. Phys. Solid. 50 (7) (2002) 1469–1510.
[37] A.G. Varias, A.R. Massih, Simulation of hydrogen embrittlement in zirconium alloys under stress and temperature gradients, J. Nucl. Mater. 279 (2) (2000) 273–285.
[38] A.G. Varias, J.L. Feng, Simulation of hydride-induced steady-state crack growth in metals–Part I: growth near hydrogen chemical equilibrium, Comput. Mech. 34 (5) (2004) 339–356.
[39] X.Q. Ma, S.Q. Shi, C.H. Woo, et al., The phase field model for hydrogen diffusion and γ-hydride precipitation in zirconium under non-uniformly applied stress, Mech. Mater. 38 (1) (2006) 3–10.
[40] X.H. Guo, S.Q. Shi, Q.M. Zhang, et al., An elastoplastic phase-field model for the evolution of hydride precipitation in zirconium. Part I: smooth specimen, J. Nucl. Mater. 378 (1) (2008) 110–119.
[41] X.H. Guo, S.Q. Shi, Q.M. Zhang, et al., An elastoplastic phase-field model for the evolution of hydride precipitation in zirconium. Part II: specimen with flaws, J. Nucl. Mater. 378 (1) (2008) 120–125.
[42] X. Gong, Y. Zhao, S. Ding, A new method to simulate the micro-thermo-mechanical behaviors evolution in dispersion nuclear fuel elements, Mech. Mater. 77 (2014) 14–27.
[43] M.P. Puls, The Effect of Hydrogen and Hydrides on the Integrity of Zirconium Alloy Components: Delayed Hydride Cracking, Springer Science & Business Media, 2012.
[44] Jingyu Zhang, et al., A theoretical model for delayed hydride cracking velocity considering the temperature history and temperature gradients, Nucl. Mater. Energy 16 (2018) 95–107.